


Connectivity and plasticity determine collagen network fracture

Federica Burla^{a,1} , Simone Dussi^{b,1}, Cristina Martinez-Torres^{a,c}, Justin Tauber^b, Jasper van der Gucht^{b,2}, and Gijse H. Koenderink^{a,c,2} 

^aBiological Soft Matter Group, Department of Living Matter, AMOLF, 1098 XG Amsterdam, The Netherlands; ^bPhysical Chemistry and Soft Matter, Wageningen University and Research, 6708 WE Wageningen, The Netherlands; and ^cDepartment of Bionanoscience, Kavli Institute of Nanoscience Delft, Delft University of Technology, 2629 HZ Delft, The Netherlands

Edited by David A. Weitz, Harvard University, Cambridge, MA, and approved February 28, 2020 (received for review November 15, 2019)

Collagen forms the structural scaffold of connective tissues in all mammals. Tissues are remarkably resistant against mechanical deformations because collagen molecules hierarchically self-assemble in fibrous networks that stiffen with increasing strain. Nevertheless, collagen networks do fracture when tissues are overloaded or subject to pathological conditions such as aneurysms. Prior studies of the role of collagen in tissue fracture have mainly focused on tendons, which contain highly aligned bundles of collagen. By contrast, little is known about fracture of the orientationally more disordered collagen networks present in many other tissues such as skin and cartilage. Here, we combine shear rheology of reconstituted collagen networks with computer simulations to investigate the primary determinants of fracture in disordered collagen networks. We show that the fracture strain is controlled by the coordination number of the network junctions, with less connected networks fracturing at larger strains. The hierarchical structure of collagen fine-tunes the fracture strain by providing structural plasticity at the network and fiber level. Our findings imply that low connectivity and plasticity provide protective mechanisms against network fracture that can optimize the strength of biological tissues.

collagen | fracture | network | connectivity

Collagen is the most abundant protein in the human body. Secreted in the extracellular space by cells, collagen assembles in networks of thick rope-like fibrils that shape and reinforce tissues and provide a scaffold for cell growth and movement (1). The spatial organization of these networks varies widely among tissues, from aligned bundles in tendons to randomly oriented (isotropic) networks in skin. Isotropic collagen networks tend to have a low connectivity, because the fibrils are mainly joined in threefold junctions by branches and in fourfold junctions by cross-links. As a result, the network connectivity is below the Maxwell criterion of six required for mechanical stability of random networks of springs (2, 3). Collagen networks nevertheless possess a finite elasticity below the percolation threshold because the fibers have a finite bending rigidity. It was recently shown that the subisostatic architecture offers a great mechanical advantage for collagen networks, because it causes them to be soft at small deformations, primarily due to fibril bending, yet stiff at large deformations, due to fibril alignment and a corresponding transition from fibril bending to stretching (3–5). Nevertheless, tissues still fracture when exposed to large deformations, especially in pathological conditions such as injuries (6), surgical interventions (7), aneurysms (8, 9), and hydraulic fracture of tumors (10, 11).

Fracture of collagen has so far mainly been investigated in tendons (12, 13), where collagen fibrils organize in long cable-like structures optimized to withstand large axial loads (14, 15). Because of the unidirectional fiber orientations, the fracture of tendons is mainly governed by molecular properties of the fibrils, which vary among functionally distinct tendons (13) and change upon age-related enzymatic cross-linking reactions (16, 17) and

during diseases (18). However, collagen in many other connective tissues assembles in disordered networks that lack a preferential orientation. Examples are skin (19), cartilage (20), vitreous humor (21), and the aortae (22). Interestingly, research on aortae fracture in the context of aneurysms (9) as well as studies using tissue models (23–26) have revealed that isotropic tissues fracture at higher strain than aligned tissues like tendon. This observation suggests that isotropic networks might be optimized to withstand larger strains, because disorder delays fracture by facilitating stress delocalization (27–31). However, a mechanistic understanding of the role of network architecture and plasticity in tissue fracture has so far been lacking, due to the complexity of living tissues.

Here, we investigate the mechanisms that protect isotropic collagen networks from fracture by performing quantitative measurements of shear-induced fracture of reconstituted collagen networks, both experimentally and computationally. Experimentally, we control the collagen structure from the network level (mesh size and connectivity) down to the fiber level (diameter and intrafibrillar cross-linking) by reconstituting networks of collagen purified from different animal and tissue sources and by exploiting the known sensitivity of collagen self-assembly to the polymerization temperature (32, 33). By comparing our results against a computational model of network fracture, we find that the connectivity of the network, defined as

Significance

Collagen fibers are the main components of the extracellular matrix, a fibrous scaffold that sets the shape and stiffness of tissues in the human body and protects them from mechanical failure. The relation between the hierarchical and heterogeneous structure of collagen networks and their fracture behavior is still missing. Prior studies focused on tendons, where collagen forms highly aligned bundles, but many tissues such as skin contain disordered collagen networks. Here, we show that fracture of disordered collagen networks is controlled by their connectivity rather than by the single-fiber properties. We further show that structural plasticity can delay network failure. Our findings are useful in understanding how tissues fail and in the design of stronger network-based materials.

Author contributions: F.B., S.D., J.v.d.G., and G.H.K. designed research; F.B., S.D., C.M.-T., and J.T. performed research; F.B., S.D., C.M.-T., J.T., J.v.d.G., and G.H.K. analyzed data; and F.B., S.D., C.M.-T., J.T., J.v.d.G., and G.H.K. wrote the paper.

The authors declare no competing interest.

This article is a PNAS Direct Submission.

Published under the [PNAS license](#).

¹F.B. and S.D. contributed equally to this work.

²To whom correspondence may be addressed. Email: jasper.vandergucht@wur.nl or g.h.koenderink@tudelft.nl.

This article contains supporting information online at <https://www.pnas.org/lookup/suppl/doi:10.1073/pnas.1920062117/-DCSupplemental>.

the mean number of fibers meeting at a junction, is the main determinant of collagen fracture. We can explain almost all of our findings by using a threshold strain for fiber fracture in the range of 10 to 20%, a value that is consistent with prior tensile tests on single collagen fibrils (34, 35). Furthermore, the computational model enables us to assess the contributions of system size and detailed network and fiber properties on the fracture behavior. Molecular effects, such as intrafibrillar cross-linking, and network properties, such as branching, modulate the fracture strain by setting the degree of plasticity. Our results are important not only for understanding how disorder protects collagen networks—and therefore, living tissues—from fracture but also for the rational design of synthetic fibrillar materials resistant to strain-induced breakage.

Results

To test the mechanical resistance of collagen networks against fracture, we perform rheology experiments on reconstituted collagen networks polymerized between the plates of a custom-built confocal rheometer. The bottom plate of the rheometer is stationary and optically transparent to allow direct visualization of changes in network structure in response to mechanical deformation using an inverted confocal microscope (Fig. 1A). In

order to assess collagen fracture, we apply a linear strain ramp γ on the networks by rotating the top plate and measuring the resulting shear stress σ . As illustrated in Fig. 1B and *SI Appendix, Fig. S1*, the stress initially increases linearly with strain, as expected for the linear elastic regime. However, above a threshold strain of 4 to 5%, the stress starts to deviate from this linear behavior and shows an upturn indicative of network stiffening. The stress eventually reaches a maximum value, which we call the peak stress σ_p , associated to a peak strain γ_p . Beyond the stress peak, the shear stress decreases, which is symptomatic of fracture. Images taken during the strain ramp at a fixed height of 20 μm above the bottom plate of the rheometer indeed reveal network fracture, as signaled by the onset of fibril motion, breakage of connections, and a decrease in fluorescence intensity in the imaging plane that signals the appearance of a crack coming from outside the field of view (Fig. 1C, *Movie S1*, and *SI Appendix, Fig. S2*). However, fracture is always first observed at strains beyond γ_p (*SI Appendix, Figs. S3 and S4*). This may be partly explained from the fact that the macroscopic strain we report here corresponds to the strain at the edge of the sample, while our imaging area is located at a radial distance halfway from the center so the local strain is only 50% of the macroscopic strain. Additionally, it is possible that cracks first form in areas outside the field of view and are observable only once they

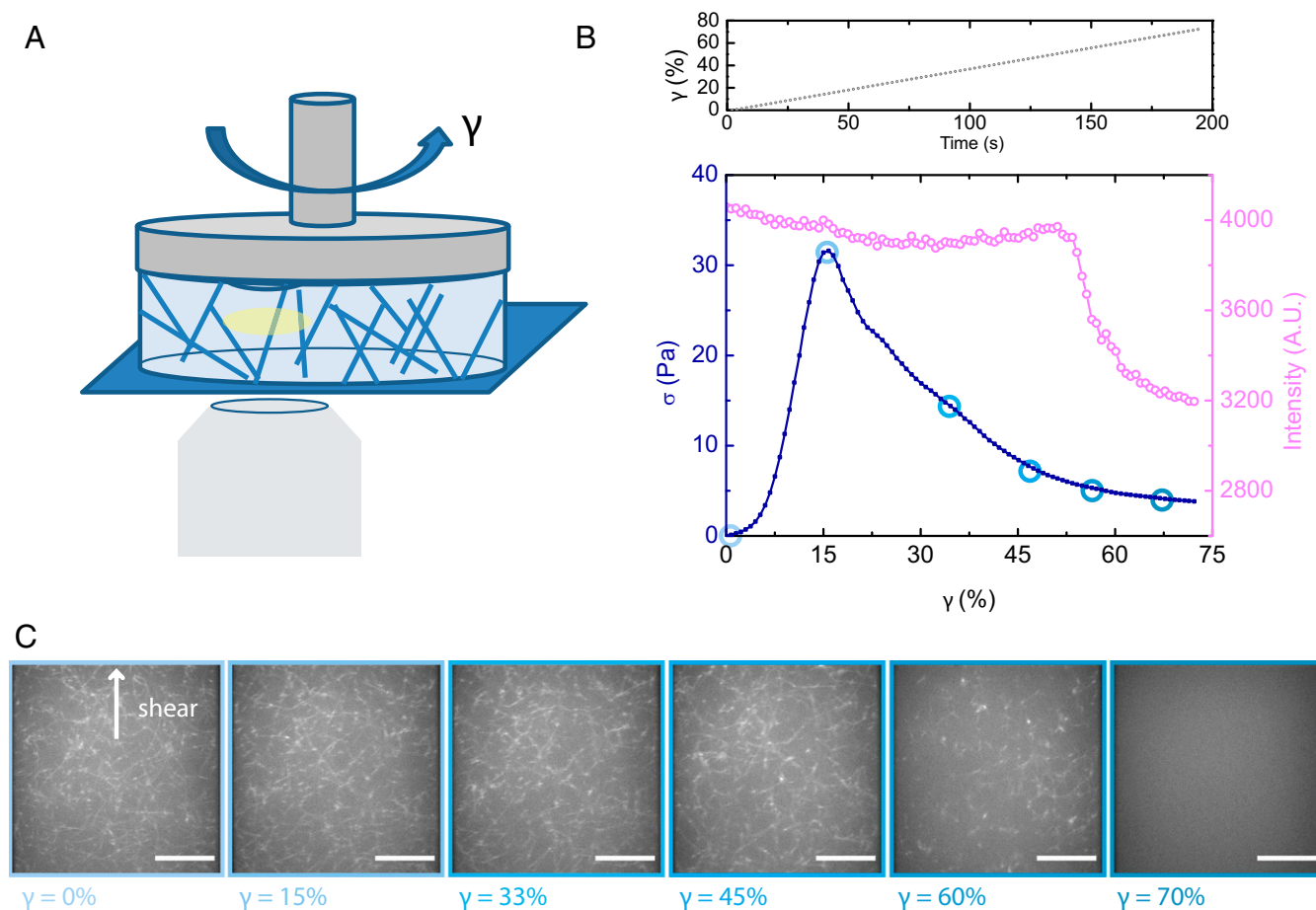


Fig. 1. Fracture of reconstituted collagen networks under shear deformation. (A) The experimental setup consists of a parallel plate rheometer with a steel top plate to apply a shear strain γ and a transparent glass bottom plate, mounted on an inverted spinning disk confocal microscope. We image a horizontal (xy) plane at a fixed distance (20 μm) away from the bottom surface (yellow-shaded region) and shifted by half of the plate radius from the center of the sample. Thus, the local strain is 50% of the strain at the edge, which is reported by the rheometer. (B) Imposed linear strain ramp (Top) and example measurement of the resulting shear stress σ (blue, left-hand y axis) as a function of shear strain γ for a 1 mg/mL network of bovine dermal telocollagen polymerized at 25 $^{\circ}\text{C}$. The total fluorescence intensity of the confocal plane is also shown (pink, right-hand y axis). (C) Confocal fluorescence images of the network labeled with eGFP-CNA35, at various strain levels (see legend) that correspond to the circles in B. (Scale bars: 10 μm .) The arrow labeled “shear” indicates the direction of shear. The data represent one repeat; more data are shown in *SI Appendix*.

propagate to the field of view. In some cases, the plane of fracture is localized above the imaging plane and we cannot observe network fracture at all. Postfracture imaging of the samples over an extended height range confirms that fracture always occurred within the bulk of the network rather than at the bottom rheometer plate (*SI Appendix, Fig. S5*).

In order to understand which structural parameters are predictive of collagen network fracture, we prepare networks with a wide range of architectures by polymerizing collagen extracted from different animal and tissue sources at different temperatures (36) (Fig. 2A). We are thus able to control the structure both at the network level (mesh size and coordination number) and at the single-fiber level (diameter) (Fig. 2B and quantification in *SI Appendix, Fig. S6*). Furthermore, we vary the fibrils' properties by comparing collagen molecules with and without telopeptide end sequences, the disordered extensions of the collagen triple helix that mediate intrafibrillar cross-linking (37). When we subject these networks to the strain ramp protocol, we measure peak strains γ_p that vary over a remarkably large range,

from 20% all of the way up to nearly 90% (Fig. 2C). The peak strains are independent of strain rate and plate diameter (*SI Appendix, Figs. S7 and S8*), again showing that the networks fail cohesively and not at the interface with the rheometer plate. We also note that changes in the surface chemistry of the plates do not significantly influence the value of the peak strain compared to its overall variation (*SI Appendix, Fig. S9*).

We do find a strong correlation between the fracture strain γ_p and the critical strain γ_c , where the networks undergo the transition from the soft bend-dominated regime to the stiff stretch-dominated regime, as shown in the *Inset* of Fig. 3A. This correlation hints at the possibility that both strains are controlled by the collagen networks' average connectivity $\langle z \rangle$ (5, 34, 36), which quantifies the distance from the rigidity percolation point and has previously been shown to control several quantities associated to the nonlinear elasticity of subisostatic networks (3, 38). Following a recently proposed method (36), we can extract $\langle z \rangle$ by mapping the nonlinear elastic response of the collagen networks onto computational predictions for subisostatic

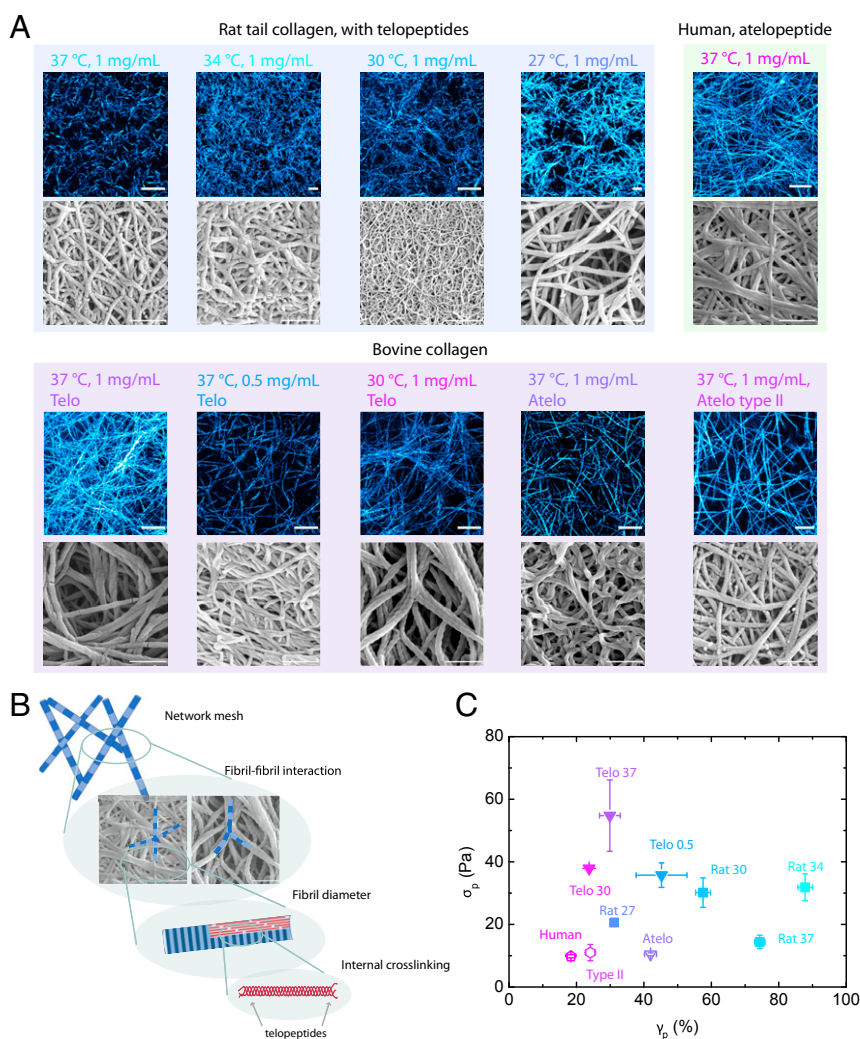


Fig. 2. The strain at which collagen networks fracture varies with network structure. (A) *Top rows*: confocal reflectance images of collagen networks. (Scale bars, 10 μm .) *Bottom rows*: corresponding scanning electron microscopy images. (Scale bars, 1 μm .) The networks were assembled from collagens from different animals, tissues, and at different temperatures (*SI Appendix, Table S1*). (B) Collagen networks possess a hierarchical structure that can differ at the network level (mesh size), fibril-fibril interaction level (junctions formed either by branching or fibril-fibril crossings), and fibril level (diameter) and molecular level (intrafibrillar cross-linking via telopeptide end regions). (C) Overview of peak strains and stresses at fracture for the entire range of collagen networks. Same symbol shapes indicate same animal and tissues; open symbols refer to collagens without telopeptides (un-cross-linked fibrils), while closed symbols refer to telocollagens (cross-linked fibrils). Peak stresses and strains are shown as averages of at least three independent repeats \pm SEM.

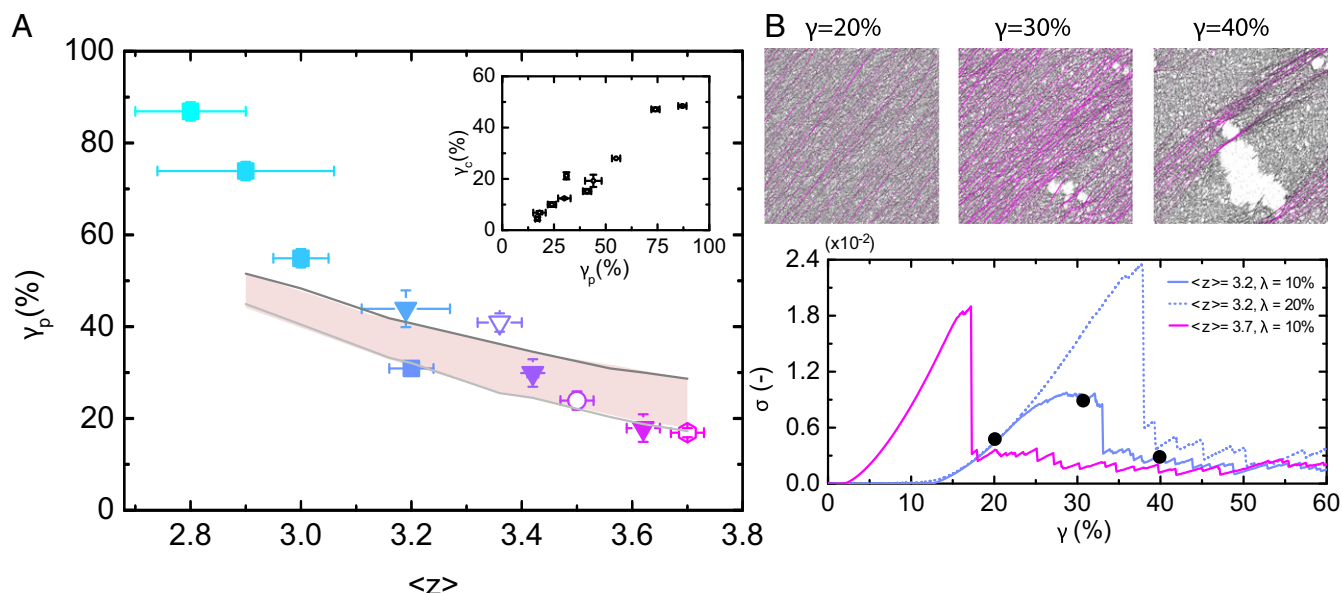


Fig. 3. Fracture experiments on collagen networks and simulations on subisostatic spring networks both show that the average network connectivity governs the rupture strain. (A) Experimentally measured (same symbols as in Fig. 2C) and simulated (lines) peak strain as a function of the average connectivity $\langle z \rangle$. The simulations were performed for two fibril rupture thresholds ($\lambda = 10\%$, lower curve, and $\lambda = 20\%$, upper curve) that bracket the physiologically relevant range. The *Inset* shows the correlation between the measured critical strain γ_c and the peak strain γ_p . Experimentally, $\langle z \rangle$ is inferred from γ_c by mapping the strain-stiffening response on simulations. (B) Example simulations of network fracture. (Upper) Simulation snapshots for a network with $\langle z \rangle = 3.2$ and $\lambda = 10\%$ at shear strains of 20% (before fracture), 30% (peak stress), and 40% (postfracture). Springs are colored according to their axial deformation (gray to pink, low to high). (Lower) Stress-strain curves for large networks ($L = 256$) with $\langle z \rangle = 3.7$ and $\lambda = 10\%$ (pink), $\langle z \rangle = 3.2$ and $\lambda = 10\%$ (solid blue), and $\langle z \rangle = 3.2$ and $\lambda = 20\%$ (dashed blue). The black circles correspond to the snapshots in the *Upper* panel.

disordered networks. We find that our collagen networks have $\langle z \rangle$ ranging between 2.9 and 3.7 (*SI Appendix, Fig. S11*). It is unfortunately impossible to directly measure $\langle z \rangle$ by imaging due to the low signal-to-noise ratio of the images, which obstructs automated junction analysis, and to the difficulty of determining whether fibers form a true junction or are merely in close proximity. Qualitatively, however, our electron microscopy data are consistent with the rheology analysis, showing that junctions are primarily formed by branches and occasional fiber crossings (*SI Appendix, Fig. S10*). Moreover, the confocal data confirm that the networks are spatially homogeneous, as indicated by a simple exponential distribution of the distance between fibers (*SI Appendix, Fig. S12*). We previously showed that internal prestresses that may build up during network polymerization can change the nonlinear mechanical properties of collagen networks (39), without changes in connectivity. We can exclude this effect here, because we observe no development of normal stresses during polymerization. We observe from Fig. 3A that the fracture strain monotonically decreases from $\sim 90\%$ for $\langle z \rangle = 2.9$ to $\sim 20\%$ for $\langle z \rangle = 3.7$ (*SI Appendix, Fig. S13*). By contrast, we observe no correlation of the fracture strain with other structural parameters that depend on the organism from which collagen is extracted, such as the fibers' diameter and bending rigidity, or the network mesh size (*SI Appendix, Fig. S14*). Our data therefore strongly suggest that the network connectivity is the dominant factor in setting the fracture strain.

This observation is consistent with recent simulations and experiments on other disordered systems, including elastic spring networks and metamaterials, whose fracture is governed by connectivity (40–43). We therefore compare our results to fracture simulations of coarse-grained fiber networks composed of L by L nodes, where each bond is modeled as an elastic spring that fractures irreversibly when its axial deformation exceeds a rupture threshold λ . We choose the computationally efficient phantom network architecture that has been proven to correctly

capture the coarse-grained features of collagen networks (3, 5, 36, 39). When we apply a shear deformation to the simulated networks, bonds align along the direction of the deformation and the network strain-stiffens (Fig. 3B), consistent with earlier findings (3, 5). In the strain-stiffening regime, the stress is heterogeneously distributed, concentrating in regions of aligned load-bearing bonds referred to as force chains. The observed mechanical disorder is a direct consequence of the subisostatic network structure, with lower average network connectivity giving rise to a more heterogeneous stress distribution (*SI Appendix, Fig. S15*). Above a threshold shear strain, bonds first start fracturing in an uncorrelated fashion and some force chains disappear, while new ones appear. When the strain reaches γ_p , an individual fracturing event triggers the formation of a large crack (see *Middle* and *Right* snapshots in Fig. 3B). Although this crack has not yet propagated through the entire sample, it does cause a large and abrupt stress drop. After the peak, the stress does not completely vanish and further small stress drops are observed, indicative of the breakage of the remaining few force chains. We notice that the damage evolution depends on the network connectivity, as detailed in *SI Appendix, Fig. S16*. By increasing $\langle z \rangle$, a smooth transition from ductile to brittle fracture is observed. For lower $\langle z \rangle$, more diffuse damage is present with microcracks slowly merging to form a spanning crack. At larger $\langle z \rangle$, the fracture process is more reminiscent of the nucleation and growth of a single large crack.

To test whether this simple model can account for the connectivity-dependent fracture of collagen network, we perform a series of simulations for networks with different $\langle z \rangle$ values spanning the experimental range and assuming a rupture threshold λ of either 10 or 20%, bracketing the range observed in single-fibril rupture experiments (34, 35). As shown in Fig. 3A, the simulations are in first instance consistent with the experimentally measured dependence of the fracture strain on connectivity. Although collagen fibers have a finite bending rigidity,

additional simulations show that fiber bending plays a negligible role, as fracture always occurs at large enough strains such that the networks are past the transition from the bending- to the stretching-dominated regime (*SI Appendix, Fig. S17*). We note that the postpeak mechanical response in simulations and experiments is different: The simulated stress-strain curves show an abrupt postpeak behavior indicative of brittle fracture (Fig. 3*B*), while the experimental stress-strain curves exhibit a more gentle, ductile fracture (*SI Appendix, Fig. S13*). The most likely origin of this difference lies in the different system sizes in experiments and simulations. To test this idea, we first verify that simulations of sheared networks reveal more brittle fracture with increasing system size (*SI Appendix, Fig. S18*), in agreement with our recent simulations of networks under uniaxial extension (43). We then perform fracture experiments for varying gap sizes and again observe a size-dependent change in ductility, even though the peak strain shows no gap size dependence for gaps larger than 200 μm (*SI Appendix, Figs. S19 and S20*), consistent with a previous study (44). Finally, we perform simulations keeping the vertical dimension L_y fixed while increasing the lateral size L_x , in order to mimic the experimental conditions where the lateral dimensions (4 cm) are almost two orders of magnitude larger than the gap size. We find that the postpeak stress-strain response is indeed smoother with increasing L_x (*SI Appendix, Figs. S19 and S21*), capturing the experimental response. Finally, we perform simulations to test whether local prestresses can influence the network response, as can be the case in colloidal gels

(45) and in other fibrous systems (46). However, as shown in *SI Appendix, Fig. S22*, we observe that in our networks the role of prestresses in controlling fracture behavior is negligible, when compared to the effects arising from changing network connectivity.

Interestingly, we notice that for low connectivity (between 2.9 and 3.0) the experimentally measured peak strain is systematically higher than the computational predictions (*SI Appendix, Fig. S23*). This discrepancy might be arising from structural plasticity in the collagen networks due to their hierarchical structure, which we have not yet considered in our computational model. Plastic mechanisms can occur either at the network level, with opening up of branches, or at the fibril level, where fibril lengthening can occur via monomer sliding (47–49) (Fig. 4*A*). We expect sliding to be particularly prominent in case of the non-cross-linked fibrils formed from collagen molecules that lack telopeptides. To experimentally test the role of fibril plasticity, we perform cyclic strain ramp tests (with a maximum strain equal to $\gamma_p/2$ to prevent fracture), comparing two bovine collagen molecules that give networks with a similar connectivity ($\langle z \rangle \sim 3.4$) but where one collagen lacks telopeptides (“atelo”), while the other has intact telopeptides (“telo”). As shown in Fig. 4*B*, we observe a larger hysteresis between the loading and unloading curves for the (non-cross-linked) atelocollagen compared to the (cross-linked) telocollagen. We also observe that the atelocollagen is softer than the telocollagen and exhibits a larger softening interval before fracture, consistent with a higher degree of plasticity

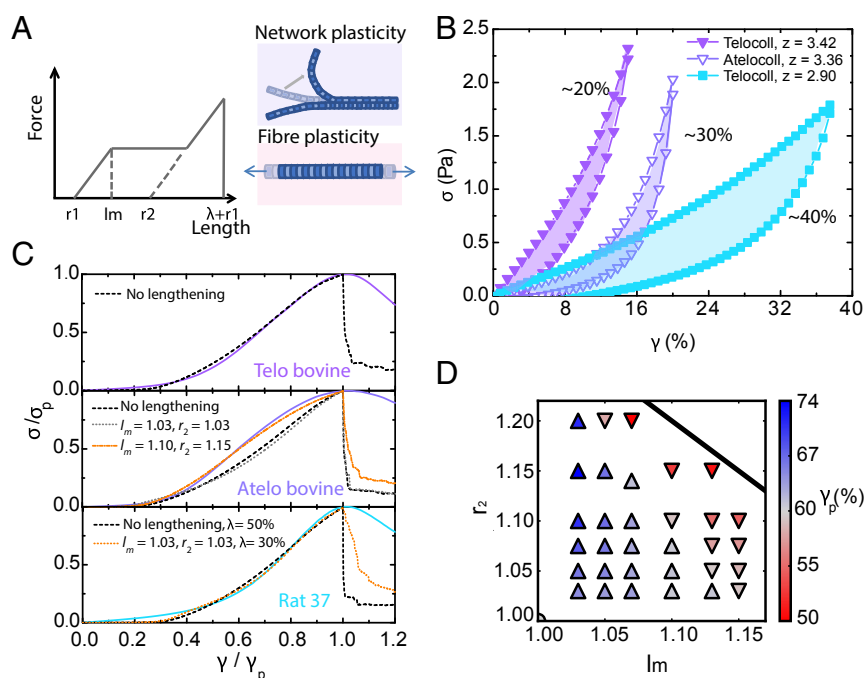


Fig. 4. The influence of structural plasticity on the fracture of collagen networks. (A) Plastic effects are implemented in the model by allowing spring lengthening based on two control parameters: the onset axial strain for fibril lengthening l_m and the increased rest length r_2 . Experimentally, plasticity can occur at the network level due to branch/bundle opening (Top schematic) and at the fiber level due to fiber lengthening (Bottom schematic). (B) Experimental shear rheology cycles measured for three different collagen networks (see legend). The normalized dissipated work W calculated from the areas under the loading and unloading curves according to $W = (A_{\text{load}} - A_{\text{unload}})/(A_{\text{load}} + A_{\text{unload}})$ is indicated next to each curve. Larger values indicate larger dissipation, meaning larger plasticity. (C) Direct comparison of normalized stress-strain curves from experiments (solid line, averaged over three samples) and from simulations (averaged over 20 configurations with $L = 256$). (Top) The response of telocollagen (Telo bovine) networks is captured by simulations of fibers that do not lengthen. (Middle) The response of atelocollagen (Atelo bovine) networks reveals significant lengthening. (Bottom) For telocollagen networks with low connectivity (Rat 37), the experimental curve matches with simulations only if we assume either an unrealistically large fiber rupture threshold λ or fiber lengthening. (D) Network peak strain γ_p of simulated networks ($L = 256, z = 2.9, \lambda = 30\%$, representative of Rat 37) as a function of l_m and r_2 . Symbols are color-coded according to the value of γ_p (see color bar). Up triangles indicate networks with an enhanced γ_p compared to the elastic limit (no lengthening), while down triangles indicate networks with a reduced γ_p . The blue line is a guide-to-the-eye separating the two regions. The area above the black line is inaccessible, because bond lengthening would occur after fiber rupture.

(SI Appendix, Fig. S24). To test for the role of plasticity at the network level, we compare two collagen networks that are both cross-linked via telopeptides but have different connectivities: telocollagen from bovine dermal skin ($\langle z \rangle = 3.42$) and rat tail collagen ($\langle z \rangle = 2.9$). In this case, a larger hysteresis between the loading and unloading curves is observed for the $\langle z \rangle = 2.9$ (rat tail) collagen compared to the $\langle z \rangle = 3.42$ (bovine) collagen, consistent with our hypothesis that branches can accommodate larger strains than cross-linked ($z = 4$) junctions.

To obtain more insight in the influence of branch and fiber plasticity on network fracture, we finally consider the shape of the stress-strain curves. We compare simulations and experiments by normalizing the curves with the peak strain γ_p and stress σ_p (Fig. 4C). After inspecting the influence of all of the simulation parameters (network connectivity, fiber rupture threshold, system size, fiber bending) on the shape of the curve (SI Appendix, Figs. S25 and S26), we choose the interval $0.6 < \gamma/\gamma_p < 0.9$ to quantify the difference between the curves and identify the simulation parameters that best capture the experimental curves. For cross-linked (telocollagen) networks at high connectivity, we find that the experiments agree well with network simulations that do not include any plastic effects (Fig. 4C, Top). By contrast, the stress-strain curves of low-connectivity and un-cross-linked (atelocollagen) networks can only be mapped onto the simulations if we allow for bond lengthening before fracture. We implement bond lengthening in the simulations by allowing the elastic springs to irreversibly extend above a lengthening threshold l_m . For simplicity, we assume that when the spring length reaches l_m , the rest length permanently changes from its initial value $r_1 = 1$ to a value $r_2 > r_1$. As before, we assume that the springs furthermore irreversibly break as soon as their deformation exceeds λ (i.e., when their length is $r_1 + \lambda$), as shown in Fig. 4A. For comparison with the experiments, we scan different combinations of l_m and r_2 and calculate the difference between the simulated and experimental stress-strain curves (after normalization) and peak strains γ_p (SI Appendix, Fig. S27). As shown in Fig. 4C, Middle, we obtain a good match between measurements on (bovine) atelocollagen networks and simulations only for $l_m \sim 1.10$. An onset strain of 10% for fiber lengthening is consistent with previous tensile measurements on isolated collagen fibrils (50–52). By contrast, for the telocollagen (rat tail) networks (Rat 37, $\langle z \rangle = 2.9$) we only find reasonable agreement with simulations for values of $l_m \sim 1.03$ (Fig. 4C, Bottom and SI Appendix, Fig. S27). This small value of l_m suggests that network-level plasticity, rather than fiber lengthening, modulates the fracture of these loosely connected ($\langle z \rangle \sim 3$) networks.

The two parameters l_m and r_2 together control the onset and degree of plastic effects due to bond lengthening in the simulations. As shown in Fig. 4D (where we fixed the rupture threshold $\lambda = 30\%$), bond lengthening only enhances the peak strain γ_p (blue up-pointing triangles) compared to the purely elastic limit in case of small l_m . By contrast, bond lengthening causes networks with larger l_m to fracture earlier (red down-pointing triangles) compared to the elastic limit. Apparently, lengthening effects are not always beneficial for delaying fracture. This can be rationalized with the fact that the stress distribution is highly inhomogeneous for networks with low connectivity, where very few bonds are highly stressed (SI Appendix, Fig. S15). Lengthening is beneficial for alleviating stress concentration in these few bonds only if lengthening already occurs at small deformation (small l_m). If the lengthening occurs at large l_m , the already high stress carried by the few bonds will not be efficiently redistributed in the network due to its low connectivity. As a consequence, these few bonds will lengthen without releasing enough stress to their neighbors so they eventually fracture. The effective rupture threshold of these bonds is therefore determined

by l_m and is lower than their intrinsic threshold λ , so the entire network will fracture earlier than in the elastic limit.

We remark that our computational study relied on treating the collagen networks as freely hinged elastic spring networks, coarse-graining therefore the discrete nature of collagen bundles and abstracting the structural complexity of the network junctions and branches. This approach allowed us to identify the main parameters controlling the fracture behavior of collagen networks, which can be generalized to other types of elastic disordered materials. For example, recent particle-based simulations on soft gels also showed heterogeneous stress distributions (53) and found that more sparsely connected networks can allow for larger deformation (45). Future studies based on less coarse-grained models than ours could further unveil the microscopic origin of the generic toughening mechanisms we identified. In particular, it would be desirable to explicitly model the hierarchical self-assembly process of collagen to reproduce the structural correlations in the network, which might be needed to more accurately describe the mechanical response of bundles and branches.

Conclusions

Collagen forms the structural scaffold of living tissues, where it is often present in the form of a disordered network of fibrils with random orientations. Large mechanical stress and pathological situations such as aneurysms can threaten the mechanical integrity of collagenous tissues. It is known that fracture of tendons, which feature a strongly anisotropic collagen structure, is governed by the molecular makeup of collagen fibers. Here, we show that fracture of isotropic collagen networks representative of tissues such as skin and cartilage is instead governed by the average connectivity $\langle z \rangle$. We find that orientational disorder combined with subisostatic connectivity protect collagen networks against fracture. This correlation between network fracture strain and connectivity is similar to that found in simpler elastic networks, such as spring networks and metamaterials. However, the hierarchical complexity of collagen does provide additional protection of collagen networks against fracture by introducing mechanisms such as branch opening or fiber lengthening that accommodate additional strain. Other parameters resulting from the different chemistries of collagen derived from different species, such as fiber diameter or mesh size, do not seem to play a role in setting the rupture strain. Our computational model provides a minimal yet powerful way to predict the role of rigidity and plasticity in setting the fracture of collagenous tissues and other fibrillar materials from first principles. Our findings provide routes to design strong fibrous materials based on the combination of a random subisostatic architecture with controlled plasticity at the network or fibril scale (54).

Materials and Methods

Sample Preparation. Collagen networks were reconstituted from commercially available collagen purified from different animal species (cow, rat, human) and from different tissues (dermis, tendon) (SI Appendix, Table S1). Moreover, we compared collagens obtained by two different extraction methods: telocollagen obtained by acid solubilization, which has intact telopeptide end sequences necessary for interfibrillar cross-linking, and atelocollagen obtained by pepsin solubilization, which lacks these telopeptides (32, 33). Finally, we also compared two different fibril-forming collagen types: type I, which is ubiquitous in all tissues except cartilage, and type II, which is characteristic of cartilage (55). All samples were prepared on ice, to prevent early collagen polymerization, by first weighing collagen in an Eppendorf tube and subsequently adding water, 10×-concentrated PBS (PBS; NaCl, 0.138 M; KCl, 0.0027 M; pH 7.4; Sigma-Aldrich), and an adequate amount of 0.1 M NaOH (sodium hydroxide; Sigma-Aldrich) in order to obtain the final desired concentration of collagen (0.5 or 1 mg/mL) in a solution of PBS and at a pH of 7.4. Each sample was subsequently vortexed for a few seconds and then quickly placed in the measurement cell (cone-plate geometry or plate-plate geometry for rheometry, glass flow cell for microscopy, Eppendorf tube for electron

microscopy) to start polymerization at the desired temperature. For the confocal rheometer experiments, we used a fluorescently tagged bacterial protein (CNA35-eGFP) that specifically binds to collagen fibrils (56) at a CNA/collagen molar ratio of 1:10.

Rheological Measurements. Strain-stiffening and fracture experiments were performed using an Anton Paar Physica MCR501 rheometer, with a stainless steel, cone-plate geometry where the cone had a 40-mm diameter and 1° cone angle. We verified the absence of wall slippage by repeating experiments with steel cone-plate cells with diameters of 20 and 30 mm. To test for gap size effects, we used plate-plate geometries with a gap of 100, 250, 500, or 750 μm and a diameter of 40 mm. Collagen solutions were allowed to polymerize for 2 h between the rheometer plates at a constant temperature (27, 30, 34, or 37 °C) maintained by a Peltier plate. During polymerization, the evolution of the linear shear moduli was monitored with a small-amplitude oscillatory strain (0.5% strain, 0.5 Hz) protocol. The steady-state values of the linear viscoelastic moduli reached after 2 h were calculated as an average over the last 10 data points of the polymerization curve. We report averages of at least three independent measurements while the error bars represent the SEM. After polymerization, the nonlinear elastic response was measured using a well-established prestress protocol (57). Briefly, a constant shear stress σ was applied for 30 s, to probe for network creep, and then an oscillatory stress $\delta\sigma$ was superposed with an amplitude of $\sigma/10$ and frequency of 0.5 Hz. The resulting differential strain $\delta\gamma$ was then used to calculate the differential (or tangent) modulus $K' = \delta\sigma/\delta\gamma$. To evaluate network fracture, we applied a linear strain ramp (with a loading rate of 0.5%/s) to the samples after polymerization. The fracture strain of each network was calculated as the strain where the stress reached a peak value. To verify that fracture occurred inside the network rather than at the plates, we performed measurements at different strain rates (0.125%/s, 1%/s, 4%/s) and we compared measurements for bare rheometer plates and for the rheometer plates coated with an adhesive layer by depositing, spreading, and drying 30 μL of a solution of fibrinogen (10 mg/mL; human plasma fibrinogen; Plasminogen; Enzyme Research Laboratories) or poly-L-lysine (poly-L-lysine solution, 0.1% [wt/vol] in H_2O ; Sigma-Aldrich) before depositing the collagen gels (58). We assessed the degree of plasticity of the collagen networks by performing repeated strain ramps and measuring the hysteresis during each stress-strain cycle. Each strain ramp was performed for strains up to $\gamma_p/2$, where γ_p was previously determined for each type of collagen.

Confocal Rheology Measurements. Confocal rheology measurements were performed on a custom-built confocal rheometer consisting of a rheometer head (DSR 301; Anton Paar) mounted in a metal rack on top of an inverted microscope (DMIRB; Leica Microsystems) equipped with a confocal spinning disk (CSU22; Yokogawa Electric Corporation). The collagen networks were imaged using a 488-nm laser (Sapphire 488-30 CHRH; Coherent) for excitation and a back-illuminated cooled EM-CCD camera (C9100; Hamamatsu Photonics) for detection. As a bottom plate, we used a circular glass coverslip (Menzel Gläser; 40 mm), which was coated beforehand with poly-L-lysine (Sigma-Aldrich) to promote attachment of the collagen network to the surface. To determine the gap size, the confocal head was manually lowered toward the glass bottom plate using a micrometer screw until the normal force increased from 0 to 0.02 N, signaling contact with the surface. Subsequently, the rheometer head was raised again from this reference point and the sample was loaded and the gap manually closed to the desired gap size. The experiments were performed at a gap of 0.5 mm and with an upper steel plate with a diameter of 20 mm. Samples were polymerized in situ at 22 °C, and solvent evaporation was prevented by placing a thin layer of mineral oil (Sigma-Aldrich) around the measuring geometry. The sample was allowed to polymerize for at least 2 h, while the elastic and viscous moduli were monitored by applying small oscillations with a strain amplitude of 0.5% and frequency of 0.5 Hz. Afterward, a linear strain ramp was applied, analogous to the standard rheology protocol described above, while the network was imaged at a confocal plane located 20 μm above the bottom surface. Time-lapse videos were collected during the strain ramp at a frame rate of 2 fps and exposure time of 500 ms. After fracture (as evident from a drop of the shear stress), we verified that the network had not detached from the lower plate by acquiring a z-stack from the bottom plate upwards, up until a height of 20 μm into the sample, and inspecting the z-stack projection from the side.

Confocal Microscopy Imaging. Confocal data for quantification of the network mesh size were obtained with an inverted Eclipse Ti microscope (Nikon) using 40 \times and 100 \times oil-immersion objectives with numerical apertures of 1.30 and 1.49, respectively (Nikon). The networks were imaged in confocal reflectance

mode with a 488-nm argon laser for illumination (Melles Griot). Image stacks were acquired starting at a height of 10 μm above the coverslip to avoid surface effects, over a total depth of 20 μm , and with a step size of 0.5 μm . The data are shown in the text as maximum intensity projections obtained with ImageJ (59). The networks were prepared in dedicated sample holders composed of two coverslips (Menzel Microscope Coverslips, 24 \times 60 mm, #1; Thermo Scientific) separated by a silicon chamber (Grace Bio-Labs CultureWell chambered coverglass; Sigma-Aldrich). The sample holders were subsequently placed in a Petri dish wrapped with humidified tissues and closed by parafilm, in order to prevent sample dehydration, and then placed in a warm room (37 °C) or in a temperature-controlled oven (for polymerization at 34 to 30 to 27 °C) to allow collagen polymerization for at least 2 h before observation.

Mesh Size Analysis. The mesh size of the collagen networks was determined with a custom-written Python code, according to a previously published protocol (60). Briefly, a z-stack of images was background subtracted, thresholded, and binarized with the Otsu method in ImageJ (59), and the Python program was used to count the distance between on and off pixels in each image, for each row and column. The distance distributions were fitted to an exponential function. The characteristic 1/e distance was converted from pixel to micrometers and taken as the average mesh size.

Scanning Electron Microscopy. The samples for scanning electron microscopy were prepared following a previously established protocol (61). Collagen networks were formed overnight in Eppendorf tubes at 0.5 or 1 mg/mL. The samples were washed three times for 60 min each with sodium cacodylate buffer (50 mM cacodylate, 150 mM NaCl, pH 7.4) obtained by mixing cacodylic acid sodium salt (Sigma-Aldrich), 0.2 M HCl, and milliQ water. The samples were fixed with 2.5% glutaraldehyde in sodium cacodylate for at least 2 h, washed again three times with cacodylate buffer at room temperature, and dehydrated with a stepwise increasing percentage of ethanol in milliQ water by sequential 10- to 20-min incubations (30, 50, 70, 80, 90, 95%). Finally, the samples were washed with 50% HDMS (hexamethyldisilazane) (Sigma-Aldrich) in ethanol and 100% HDMS. HDMS was pipetted out, and the Eppendorf tubes were left open overnight in order to dry. Subsequently, the samples were mounted on a support with carbon tape and covered with a 11- to 14-nm layer of palladium gold with a sputter-coater (Leica; EM ACE600). The samples were then imaged with a scanning electron microscope (Verios 460; FEI). To determine the fibril diameters, we manually analyzed images taken at a magnification of 80,000 \times , by drawing segments perpendicular to a collagen fibril and then measuring the distance between the edges. To prevent bias, we overlaid a grid of 500 \times 500 nm onto each image through the ImageJ grid plugin, and measured the fibrils at the intersections of the crosses. We note that the measured fibril diameters are semiquantitative because the sample preparation for electron microscopy introduces fibril shrinkage from drying but also fibril thickening due to metal deposition, while imaging in vacuum also introduces fibril shrinkage. This does not influence our conclusions, because the diameter data are only used as a relative measure between different collagen networks.

Determination of Onset and Critical Strain for Collagen Strain-Stiffening. The nonlinear rheology data (differential elastic modulus K' as a function of shear stress σ) were evaluated using a custom-written Python routine. The onset stress was determined by considering the minimum value of the experimentally determined K'/σ as a function of σ . The corresponding strain was defined as onset strain γ_o . To determine the critical strain, we calculated the cubic spline derivative of $\log K'$ as a function of $\log \gamma$. The strain at which this function reached its maximum was defined the critical strain γ_c . The characteristic strain values are shown as averages with SEM of at least three independent measurements.

Determination of Structural and Mechanical Properties of Collagen from Rheology Data. It was previously shown that the nonlinear elastic response of collagen networks is quantitatively described by a theoretical model of athermal networks of rigid beams (3, 36). Specifically, the increase of the differential modulus K' with increasing shear strain γ obeys the following equation of state:

$$\frac{\bar{\kappa}}{|\Delta\gamma|^\Phi} \sim \frac{K'}{|\Delta\gamma|^\Gamma} \left(\pm 1 + \frac{K'^{\frac{1}{\Gamma}}}{|\Delta\gamma|^\Gamma} \right)^{(\Phi-\Gamma)}, \quad [1]$$

where $\bar{\kappa}$ represents the dimensionless bending rigidity, defined as the ratio between the fiber bending modulus κ and stretch modulus μ , $|\Delta\gamma|$ is the

distance between the measured strain and the critical strain γ_c and φ and f are critical exponents controlling the transition from the bend-dominated to the stretch-dominated regime. The critical strain and the critical exponents depend on the network architecture through its average connectivity $\langle z \rangle$ and can be determined from computer simulations of two-dimensional random lattice-based networks (36). From this same comparison between experiments and simulations, we could also obtain the corresponding values of f and φ . Next, we used these parameters as input to fit the experimental strain-stiffening curves to Eq. 1, using the dimensionless bending rigidity of the fibers $\bar{\kappa}$ as the fitting parameter (SI Appendix, Table S2).

Computer Simulations of Fiber Networks. We performed athermal and quasistatic shear simulations of elastic networks composed of L by L nodes (or L_x by L_y nodes in cases where the simulation box was asymmetric). In line with previous studies (3, 5, 36, 39), we chose a phantom network architecture that has been proven to capture the essential coarse-grained features controlling the mechanics of collagen networks. The phantomization procedure is as follows: 1) starting from a triangular lattice with unit spacing, only two of the three fibrils meeting at the same node are cross-linked; 2) for each fibril, at least one segment is randomly removed to avoid unphysical system-spanning bonds; 3) the desired average connectivity $\langle z \rangle$ is achieved by diluting the network, i.e., by randomly removing a fraction $1 - p$ of bonds, yielding $\langle z \rangle = 4p$. In the simplest model considered in this study, each bond was modeled as an elastic linear (Hookean) spring with unit stiffness and rest length equal to the lattice spacing (set to unity). All springs have the same rupture threshold λ and break irreversibly when their deformation exceeds λ . As shown in SI Appendix, we also performed simulations where we included a three-body bending potential along straight segments, to test whether the fibril bending stiffness κ has any effect on network fracture. These simulations were performed in a similar manner as in previous studies (3), but with the addition of bond rupture events when the axial deformation of a spring exceeded λ . To test for the influence of fibril plasticity, we finally performed simulations where we allowed for spring lengthening: as soon as the spring length reaches l_m , its rest length increases to r_2 . The relation $l_m + r_2 - 2r_1 < \lambda$ must hold; otherwise, spring lengthening would occur after bond rupture

(inaccessible region above the line in Fig. 4D). In all cases, networks were subjected to a simple shear deformation. After each small increment of the shear strain γ , the energy was minimized using the FIRE algorithm (62), with a tolerance (in reduced units) $F_{rms} \leq 10^{-5}$, ensuring that simulations were carried out in the athermal limit. Bonds were broken one at a time (if any), starting from the weakest (the one that exceeded λ the most) and performing energy minimization in between fracture events. Lee-Edwards boundary conditions were employed, except in the case of strongly asymmetric boxes ($L_x \gg L_y$), for which the top and bottom boundary nodes were moved rigidly (to avoid unphysical elastic waves traveling through the system when bonds are fracturing). Laterally (in the x direction), standard periodic boundary conditions were always employed. The mechanical response was quantified via the shear stress σ calculated using the xy component of the virial stress tensor. Quantities (σ and K') were expressed in reduced units and averaged over a sufficiently large number of configurations, ranging from 500 for $L = 24$ to 20 for $L = 256$.

Data Availability. The data discussed in the paper are available from the corresponding authors upon request.

ACKNOWLEDGMENTS. We gratefully acknowledge F. C. MacKintosh (Rice University) for extensive scientific discussions and M. Dompè (Wageningen University and Research) for a critical reading of the manuscript. We furthermore thank M. van Hecke (AMOLF/Leiden University) for kindly lending us the confocal rheometer head and for critically reading the manuscript; M. Verweij, J. B. Aans and D.-J. Spaanderman (AMOLF) for help with designing and building the confocal rheometer; and M. Vinkenoog (AMOLF) for help with CNA35 protein purification. The work of F.B. and G.H.K. is part of the Industrial Partnership Programme Hybrid Soft Materials that is carried out under an agreement between Unilever Research and Development B.V. and the Netherlands Organisation for Scientific Research. The work of S.D., J.T., and J.v.d.G. is part of the SOFTBREAK project funded by the European Research Council (European Research Council Consolidator Grant). C.M.T. was supported by an NWO-Veni-2017 grant from the Netherlands Organisation for Scientific Research.

1. J. K. Mouw, G. Ou, V. M. Weaver, Extracellular matrix assembly: A multiscale deconstruction. *Nat. Rev. Mol. Cell Biol.* **15**, 771–785 (2014).
2. J. C. Maxwell, On the calculation of the equilibrium and stiffness of frames. *Lond. Edinb. Dublin Philos. Mag. J. Sci.* **27**, 294–299 (1864).
3. A. Sharma et al., Strain-controlled criticality governs the nonlinear mechanics of fibre networks. *Nat. Phys.* **12**, 584–587 (2016).
4. F. Burla, Y. Mulla, B. E. Vos, A. Aufderhorst-Roberts, G. H. Koenderink, From mechanical resilience to active material properties in biopolymer networks. *Nat. Rev. Phys.* **1**, 249–263 (2019).
5. A. J. Licup et al., Stress controls the mechanics of collagen networks. *Proc. Natl. Acad. Sci. U.S.A.* **112**, 9573–9578 (2015).
6. A. S. LaCroix, S. E. Duenwald-Kuehl, R. S. Lakes, R. Vanderby, Jr, Relationship between tendon stiffness and failure: A metaanalysis. *J. Appl. Physiol.* **115**, 43–51 (2013).
7. M. I. Converse et al., Detection and characterization of molecular-level collagen damage in overstretched cerebral arteries. *Acta Biomater.* **67**, 307–318 (2018).
8. M. Anne et al., Diversity in the strength and structure of unruptured cerebral aneurysms. *Ann. Biomed. Eng.* **25**, 289–313 (2016).
9. S. Sugita, T. Matsumoto, Local distribution of collagen fibers determines crack initiation site and its propagation direction during aortic rupture. *Biomech. Model. Mechanobiol.* **17**, 577–587 (2018).
10. Q. D. Tran, Marcos, D. Gonzalez-Rodriguez, Permeability and viscoelastic fracture of a model tumor under interstitial flow. *Soft Matter* **14**, 6386–6392 (2018).
11. M. Arroyo, X. Trepas, Hydraulic fracturing in cells and tissues: Fracking meets cell biology. *Curr. Opin. Cell Biol.* **44**, 1–6 (2017).
12. S. P. Veres, J. M. Harrison, J. M. Lee, Repeated subrupture overload causes progression of nanoscaled discrete plasticity damage in tendon collagen fibrils. *J. Orthop. Res.* **31**, 731–737 (2013).
13. T. W. Herod, N. C. Chambers, S. P. Veres, Collagen fibrils in functionally distinct tendons have differing structural responses to tendon rupture and fatigue loading. *Acta Biomater.* **42**, 296–307 (2016).
14. P. Fratzl, R. Weinkamer, Nature's hierarchical materials. *Prog. Mater. Sci.* **52**, 1263–1334 (2007).
15. M. J. Buehler, Y. C. Yung, Deformation and failure of protein materials in physiologically extreme conditions and disease. *Nat. Mater.* **8**, 175–188 (2009).
16. R. B. Svensson, H. Mulder, V. Kovanen, S. P. Magnusson, Fracture mechanics of collagen fibrils: Influence of natural cross-links. *Biophys. J.* **104**, 2476–2484 (2013).
17. R. B. Svensson, S. T. Smith, P. J. Moyer, S. P. Magnusson, Effects of maturation and advanced glycation on tensile mechanics of collagen fibrils from rat tail and Achilles tendons. *Acta Biomater.* **70**, 270–280 (2018).
18. K. Misof, W. J. Landis, K. Klaushofer, P. Fratzl, Collagen from the osteogenesis imperfecta mouse model (oim) shows reduced resistance against tensile stress. *J. Clin. Invest.* **100**, 40–45 (1997).
19. J. F. Ribeiro, E. H. M. dos Anjos, M. L. S. Mello, B. de Campos Vidal, Skin collagen fiber molecular order: A pattern of distributional fiber orientation as assessed by optical anisotropy and image analysis. *PLoS One* **8**, e54724 (2013).
20. K. Meng et al., The effect of collagen fibril orientation on the biphasic mechanics of articular cartilage. *J. Mech. Behav. Biomed. Mater.* **65**, 439–453 (2017).
21. K. J. Bos et al., Collagen fibril organisation in mammalian vitreous by freeze etch/rotary shadowing electron microscopy. *Micron* **32**, 301–306 (2001).
22. J. H. N. Lindeman et al., Distinct defects in collagen microarchitecture underlie vessel-wall failure in advanced abdominal aneurysms and aneurysms in Marfan syndrome. *Proc. Natl. Acad. Sci. U.S.A.* **107**, 862–865 (2010).
23. S. M. Vanderheiden, M. F. Hadi, V. H. Barocas, Crack propagation versus fiber alignment in collagen gels: Experiments and multiscale simulation. *J. Biomech. Eng.* **137**, 121002 (2015).
24. M. F. Hadi, V. H. Barocas, Microscale fiber network alignment affects macroscale failure behavior in simulated collagen tissue analogs. *J. Biomech. Eng.* **135**, 021026 (2013).
25. R. Y. Dhume, E. D. Shih, V. H. Barocas, Multiscale model of fatigue of collagen gels. *Biomech. Model. Mechanobiol.* **18**, 175–187 (2019).
26. K. Bircher, M. Zündel, M. Pensalfini, A. E. Ehret, E. Mazza, Tear resistance of soft collagenous tissues. *Nat. Commun.* **10**, 1–13 (2019).
27. M. J. Alava, P. K. V. V. Nukala, S. Zapperi, Statistical models of fracture. *Adv. Phys.* **55**, 349–476 (2006).
28. S. Patinet, D. Vandembroucq, A. Hansen, S. Roux, Cracks in random brittle solids. *Eur. Phys. J. Spec. Top.* **223**, 2339–2351 (2014).
29. A. Shekhawat, S. Zapperi, J. P. Sethna, From damage percolation to crack nucleation through finite size criticality. *Phys. Rev. Lett.* **110**, 185505 (2013).
30. L. Ponson, D. Bonamy, E. Bouchaud, Two-dimensional scaling properties of experimental fracture surfaces. *Phys. Rev. Lett.* **96**, 035506 (2006).
31. A. Garcimartin, A. Guarino, L. Bellon, S. Ciliberto, Statistical properties of fracture precursors. *Phys. Rev. Lett.* **79**, 3202–3205 (1997).
32. S. Leikin, D. C. Rau, V. A. Parsegian, Temperature-favoured assembly of collagen is driven by hydrophilic not hydrophobic interactions. *Nat. Struct. Biol.* **2**, 205–210 (1995).
33. W. Traub, Molecular assembly in collagen. *FEBS Lett.* **92**, 114–120 (1978).
34. M. Guthold et al., A comparison of the mechanical and structural properties of fibrin fibers with other protein fibers. *Cell Biochem. Biophys.* **49**, 165–181 (2007).
35. S. M. A. Iqbal, D. Deska-Gauthier, L. Kreplak, Assessing collagen fibrils molecular damage after a single stretch-release cycle. *Soft Matter* **15**, 6237–6246 (2019).
36. K. A. Jansen et al., The role of network architecture in collagen mechanics. *Biophys. J.* **114**, 2665–2678 (2018).
37. M. Shayegan, T. Altindal, E. Kiefl, N. R. Forde, Intact telopeptides enhance interactions between collagens. *Biophys. J.* **111**, 2404–2416 (2016).
38. C. P. Broeders, X. Mao, T. C. Lubensky, F. C. MacKintosh, Criticality and isostaticity in fibre networks. *Nat. Phys.* **7**, 983–988 (2011).

39. F. Burla, J. Tauber, S. Dussi, J. van der Gucht, G. H. Koenderink, Stress management in composite biopolymer networks. *Nat. Phys.* **15**, 549–553 (2019).
40. L. Zhang, D. Z. Rocklin, L. M. Sander, X. Mao, Fiber networks below the isostatic point: Fracture without stress concentration. *Phys. Rev. Mater.* **1**, 1–5 (2017).
41. M. M. Driscoll et al., The role of rigidity in controlling material failure. *Proc. Natl. Acad. Sci. U.S.A.* **113**, 10813–10817 (2016).
42. E. Berthier et al., Rigidity percolation control of the brittle-ductile transition in disordered networks. *Phys. Rev. Mater.* **075602**, 1–9 (2019).
43. S. Dussi, J. Tauber, J. van der Gucht, Athermal fracture of elastic networks: How rigidity challenges the unavoidable size-induced brittleness. *Phys. Rev. Lett.* **124**, 018002 (2020).
44. R. C. Arevalo, J. S. Urbach, D. L. Blair, Size-dependent rheology of type-I collagen networks. *Biophys. J.* **99**, L65–L67 (2010).
45. M. Bouzid, E. Del Gado, Network topology in soft gels: Hardening and softening materials. *Langmuir* **34**, 773–781 (2018).
46. D. Feng et al., Disease-causing mutation in α -actinin-4 promotes podocyte detachment through maladaptation to periodic stretch. *Proc. Natl. Acad. Sci. U.S.A.* **115**, 1517–1522 (2018).
47. S. Münster et al., Strain history dependence of the nonlinear stress response of fibrin and collagen networks. *Proc. Natl. Acad. Sci. U.S.A.* **110**, 12197–12202 (2013).
48. E. Ban et al., Mechanisms of plastic deformation in collagen networks induced by cellular forces. *Biophys. J.* **114**, 450–461 (2018).
49. J. Liu et al., Energy dissipation in mammalian collagen fibrils: Cyclic strain-induced damping, toughening, and strengthening. *Acta Biomater.* **80**, 217–227 (2018).
50. B. Depalle, Z. Qin, S. J. Shefelbine, M. J. Buehler, Influence of cross-link structure, density and mechanical properties in the mesoscale deformation mechanisms of collagen fibrils. *J. Mech. Behav. Biomed. Mater.* **52**, 1–13 (2015).
51. P. Fratzl et al., Fibrillar structure and mechanical properties of collagen. *J. Struct. Biol.* **122**, 119–122 (1998).
52. R. Puxkandl et al., Viscoelastic properties of collagen: Synchrotron radiation investigations and structural model. *Philos. Trans. R. Soc. Lond. B Biol. Sci.* **357**, 191–197 (2002).
53. J. Colombo, E. Del Gado, Stress localization, stiffening, and yielding in a model colloidal gel. *J. Rheol. (N.Y.N.Y.)* **58**, 1089–1116 (2014).
54. E. Prince, E. Kumacheva, Design and applications of man-made biomimetic fibrillar hydrogels. *Nat. Rev. Mater.* **4**, 99–115 (2019).
55. S. Ricard-Blum, The collagen family. *Cold Spring Harb. Perspect. Biol.* **3**, a004978 (2011).
56. S. J. A. Aper et al., Colorful protein-based fluorescent probes for collagen imaging. *PLoS One* **9**, e114983 (2014).
57. C. P. Broedersz et al., Measurement of nonlinear rheology of cross-linked biopolymer gels. *Soft Matter* **6**, 4120–4127 (2010).
58. S. Nam, K. H. Hu, M. J. Butte, O. Chaudhuri, Strain-enhanced stress relaxation impacts nonlinear elasticity in collagen gels. *Proc. Natl. Acad. Sci. U.S.A.* **113**, 5492–5497 (2016).
59. J. Schindelin et al., Fiji: An open-source platform for biological-image analysis. *Nat. Methods* **9**, 676–682 (2012).
60. L. J. Kaufman et al., Glioma expansion in collagen I matrices: Analyzing collagen concentration-dependent growth and motility patterns. *Biophys. J.* **89**, 635–650 (2005).
61. T. C. Baradet, J. C. Haselgrove, J. W. Weisel, Three-dimensional reconstruction of fibrin clot networks from stereoscopic intermediate voltage electron microscope images and analysis of branching. *Biophys. J.* **68**, 1551–1560 (1995).
62. E. Bitzek, P. Koskinen, F. Gähler, M. Moseler, P. Gumbsch, Structural relaxation made simple. *Phys. Rev. Lett.* **97**, 170201 (2006).